Dynamics of acetone photodissociation: a surface hopping study.

Lucilla Favero

Università di Pisa, Dipartimento di Farmacia,

via Bonanno Pisano 33, 56126 Pisa, Italy

Giovanni Granucci and Maurizio Persico

Università di Pisa, Dipartimento di Chimica e Chimica Industriale,

via Risorgimento 35, 56126 Pisa, Italy

Abstract

We present on the fly surface hopping simulations of the dynamics of photoexcited acetone in the $n \rightarrow \pi^*$ band, taking into account both the spin-orbit and the dynamic couplings and allowing for the C-C bond dissociation. The S_0, S_1, T_1 and T_2 states were considered and the propagation time was 50 ps. According to the simulation results, after excitation to S_1 both Internal Conversion (IC) to S_0 and InterSystem Crossing (ISC) to T_1 or T_2 take place at comparable rates; T_2 plays an important role and the simultaneous treatment of the spin-orbit and dynamic couplings is shown to be mandatory to describe the photodynamics. We propose a mechanism that explains the observed fast and slow decay rates of the S_1 state of acetone.

Keywords: Acetone - Photodissociation - InterSystem Crossing - Internal Conversion - Surface Hopping - Spin-orbit coupling

1   Introduction

The cleavage of the α-CC bond in ketones after photoexcitation is called Norrish type-I reaction [1], and has been extensively studied both experimentally and theoretically, expecially for the simplest ketone, acetone [2–26]. Around the ground state equilibrium geometry the S_1 and T_1 states have $n \rightarrow \pi^*$ character and therefore are close lying in energy. The $S_0 \rightarrow S_1$ transition is symmetry forbidden and gives rise to a weak and broad band from 330 to 220 nm, with a maximum around 275 nm, corresponding to an excitation energy $\Delta E_{exc} = 4.51$ eV [27, 28]; the S_1 state is bound and its band origin at $\Delta E_{exc} = 3.773$ is higher, but very close, to the C-C bond dissociation energy, $D_0 = 3.60 \pm 0.02$ eV [29]. For multiple reasons (the need to transfer the excitation from the carbonyl group to the C-C bond, the small energy excess available for dissociation, the proximity of the triplet state), assessing the mechanism of acetone photodissociation after excitation in the $n \rightarrow \pi^*$ band is not straightforward, and was long debated.

Three research groups [2–4] measured the time-resolved photoionization by mass spectroscopy detection, following photoexcitation at 4.63–4.79 eV. Their transient is in the 100 fs time scale, so an ultrafast (< 200 fs) C-C bond breaking on the S_1 surface was initially proposed [2,3]. These findings were recently reinterpreted by Sølling and coworkers, who combined experimental work and wavepacket dynamics simulations [5,6]. In particular, they showed that the ultrafast decay of the ion signal is due to the initial motion of the wavepacket on the S_1 surface, away from the Franck-Condon region [6]. Moreover, with ΔE_{exc} in the 4.3–4.9 eV range, they found that two time-resolved photoionization signals, associated with the $(CH_3)_2CO^+$ and the CH_3CO^+ ions, exhibit long tails (very weak and with low signal/noise ratios), still present after 100 ps [5]. The authors assigned such tails to the vibrationally relaxed S_1 state, the lifetime of which would then be much longer than 100 ps. This is in agreement with the CH_3CO photofragment detection by photoionization [4, 7]; in fact, this signal kept increasing in intensity during the whole pump-probe delay interval, i.e. up to 120 ps after 307 nm excitation ($\Delta E_{exc} = 4.039$ eV). Haas and coworkers measured the fluorescence transients over a time scale of a few μs [8–10]. They found a decay with a fast and a slow component, the former corresponding to a lifetime τ_{fast} shorter than the experimental resolution of 10 ns. The importance of the fast component increases with the exciting photon energy ΔE_{exc}: it is absent near the band origin (3.773 eV), it manifests itself at about 3.9 eV and dominates above 4 eV, so that at high energies the long tail is of minor importance. The long lifetime, τ_{slow}, depends on ΔE_{exc} and is also influenced by deuteration and by collisions (i.e. molecular beam versus rarefied gas). For low ΔE_{exc}, τ_{slow} is approximately in the range 1–5 μs. When ΔE_{exc} exceeds 4.052 eV for $(CH_3)_2CO$ or 4.083 eV for $(CD_3)_2CO$, τ_{slow} sharply decreases to much smaller values; this threshold was interpreted as the onset of dissociation in the T_1 state, following InterSystem Crossing (ISC).

After the first C-C bond breaking, the acetyl radical can further fragment to CH_3 + CO. In experiments with $\Delta E_{exc} = 5.00$ eV, the CO quantum yield was found to decrease with the buffer gas pressure, starting from about 0.5 at the lowest pressure (25 mbar) [11, 12]. The pressure dependence was attributed to vibrational quenching of CH_3CO, preventing its dissociation. By assuming dissociation in the T_1 potential energy surface (PES), Martínez-Núñez and coworkers [13] ran classical trajectory simulations and were able to reproduce the experimental energy distributions for CH_3, CH_3CO and CO, as obtained by excitation with $\Delta E_{exc} = 4.66$, 5.00 or 6.42 eV [14–16]. However, a fraction of the acetone molecules excited at $\Delta E_{exc} = 5.00$ eV do not undergo the Norrish type-I cleavage: in fact, direct measurements of CH_3CO by pulsed laser spectroscopy

found a value of $\Phi_{diss} \simeq 0.5$ for the photodissociation quantum yield, upon extrapolation to zero buffer gas pressure [17]. Other studies showed that Φ_{diss} also depends on the excitation wavelength λ_{exc} [18–20]. Through rather complex kinetic models taking into account collisional quenching, the authors concluded that the triplet quantum yield Φ_{ISC}, also extrapolated to low buffer gas pressure, goes from almost 1 at $\Delta E_{exc} = 3.75 - 3.90$ eV to practically zero above $\Delta E_{exc} \simeq 4.1$ eV [18, 19]. The Stern-Volmer plots obtained by Blitz et al. [19] are linear at $\Delta E_{exc} = 4.397$ eV and non-linear (much steeper) at 3.936 or 4.025 eV. This was interpreted as the onset of dissociation on the S_1 PES around $\Delta E_{exc} = 4.1 - 4.2$ eV, while below this threshold only the T_1 mechanism would be viable. In similar experiments, Szilágyi et al. found a curvature at low pressures with $\Delta E_{exc} = 4.025$ eV, and evaluated the triplet quantum yield at about 0.5 [20]. Finally, DC slice imaging experiments, conducted after photoexcitation in the upper end of the $n \to \pi^*$ band of acetone ($\Delta E_{exc} = 5.39$ eV) by Goncharov et al. [21], showed a bimodal translational energy distribution of the CO product, interpreted as the signature of two mechanisms: the stepwise one that operates after ISC to T_1, and a "roaming" dissociation mechanism, in which the reaction takes place on the S_0 surface, giving rise to translationally and rotationally cold CO and vibrationally hot ethane.

In the present contribution, we report mixed quantum-classical surface hopping (SH) simulations of acetone dynamics after $n \to \pi^*$ photoexcitation. Our aim is to clarify the mechanism of the C-C cleavage, expecially concerning the role of the triplet state T_1, and the S_1 lifetime. In our SH simulations all the nuclear degrees of freedom were taken into account and the electronic wavefunctions and couplings (dynamic and spin-orbit) were obtained on the fly. To this aim we applied a semiempirical method, reparameterized mainly on the basis of new ab initio multi-reference configuration interaction (MRCI) calculations (see section 2). Both internal conversion (IC) and intersystem crossing (ISC) processes were explicitly considered; we are not aware of any previous molecular dynamics simulation aimed at unravel the importance and the mechanism of ISC in acetone photodissociation. According to El-Sayed's selection rules [30], the spin-orbit (SO) coupling between S_1 and T_1 is expected to be very small at short C-C distances. The singlet-triplet SO interaction is gradually transformed in an effective doublet-doublet coupling along the reaction coordinate, and this has to be taken into account in the dynamics: simulations based on a constant (independent on nuclear coordinates) value of the SO coupling are not likely to yield meaningful results. On the other hand, the $S_1 \to T_1$ ISC could be promoted by the coupling with the $\pi \to \pi^*$ T_2 state, which has a larger SO interaction with S_1. For this reason T_2 was included in the dynamics simulations presented here.

2   Potential energy surfaces

The first two singlet (S_0, S_1) and triplet (T_1, T_2) electronic states of acetone were characterized by performing ab initio MRCI (with singles and doubles excitations) on top of state-averaged CASSCF (SA-CAS) calculations. The active space comprised 6 electrons in 5 orbitals, represented, around the equilibrium geometries of the states considered, by the σ, π, π^* and σ^* orbitals of the CO group, and one lone pair of the oxygen atom. In the SA-CAS procedure the four states had equal weights. In the MRCI calculations the four core orbitals were frozen. The Gaussian basis set considered was cc-pVTZ for C and O and cc-pVDZ for H. As the states we are considering are largely valence in nature, diffuse functions were not added [31]. Only single point calculations were done at MRCI level: for geometry optimizations and for the search of minimum energy conical

Table 1: Energies (eV) at critical points for the first two singlet and triplet states of acetone. All energies are relative to the S_0 minimum with the same method. MXS labels a minimum energy conical intersection.

	SA-CAS[a]	MRCI[a]	MR-CISD+Q[b]	NEVPT2[c]	CASPT2[d]	Exp
S_0 minimum	0	0	0	0	0	
$E(S_1) - E(S_0)$	4.501	4.498	4.54	4.47	4.304	4.5[e]
$E(T_1) - E(S_0)$	4.174	4.168		4.11		
$E(T_2) - E(S_0)$	5.879	6.080				
S_1 minimum	3.534	3.792	3.74	3.75	3.615	3.815[f]
$E(S_1) - E(S_0)$	2.200	2.336	2.58			2.88[g]
T_1 minimum	3.330	3.543		3.49	3.395	
$E(T_1) - E(S_0)$	2.093	2.195				2.65[g]
T_2 minimum	4.177	4.521		4.48		
$E(T_2) - E(S_0)$	2.306	2.475				
S_0/S_1 MXS	4.843	4.888/4.940	4.78		4.699	
S_1/T_1 MXS	4.502	4.905/4.864			5.172	
$CH_3CO + CH_3$						
S_0 and T_1 min.	3.497	3.742	3.39		3.581	3.83[h]
S_1 and T_2 min.	4.876	5.031	4.75		4.865	

[a] This work. [b] Ref. [23]. [c] Refs. [34, 37]. [d] Ref. [24]. [e] Maximum of the gas phase absorption spectrum [27,35,36]. [f] S_1 band origin (3.773 eV), supersonic jet [28] corrected for the ZPE difference (with ZPEs taken from ref. [37]). [g] Maximum of the gas phase fluorescence/phosphorescence spectrum, room temperature [20]. [h] From the reaction enthalpy (3.60 eV), corrected for the ZPE difference [29].

intersections (MXS), SA-CAS was used. All these calculations were performed with the program package COLUMBUS [32] (with the exception of the S_1/T_1 MXS search, for which we used MOLPRO [33])

In Table 1 we show the relative energies of the four states at their equilibrium and dissociated geometries. At the S_0 minimum, the acetone molecule belongs to the C_{2v} symmetry group and the four states are, in energetic order, X^1A_1, $^3A_2$, $^1A_2$ and $^3A_1$. As expected after $n \to \pi^*$ or $\pi \to \pi^*$ excitations, the equilibrium geometries of T_1, S_1 and T_2 display elongated C-O bond and pyramidalization at the central carbon atom (see Table 2) giving rise to broad absorption and emission bands, with sizeable Stokes shifts. The MRCI values for both the adiabatic S_1-S_0 energy difference and the vertical transition energy at the S_0 minimum compare well with the spectroscopic data, i.e. the origin and the maximum of the absorption band. On the other hand, the computed vertical $S_1 - S_0$ and $T_1 - S_0$ energy differences at the equilibrium geometries of the excited states are both about 0.5 eV lower than the maxima in the fluorescence and phosphorescence spectra, $h\nu_{max}$. Actually, the vertical transition energy corresponds only approximately to the maximum Franck-Condon factor, which in turn is found at an estimated 0.15 eV less

Table 2: Selected geometrical parameters at critical points for the first two singlets and triplets of acetone and for the acetyl fragment, from SA-CAS optimizations. Distances in Å, angles in degree. The full set of cartesian coordinates is given in the supporting informations.

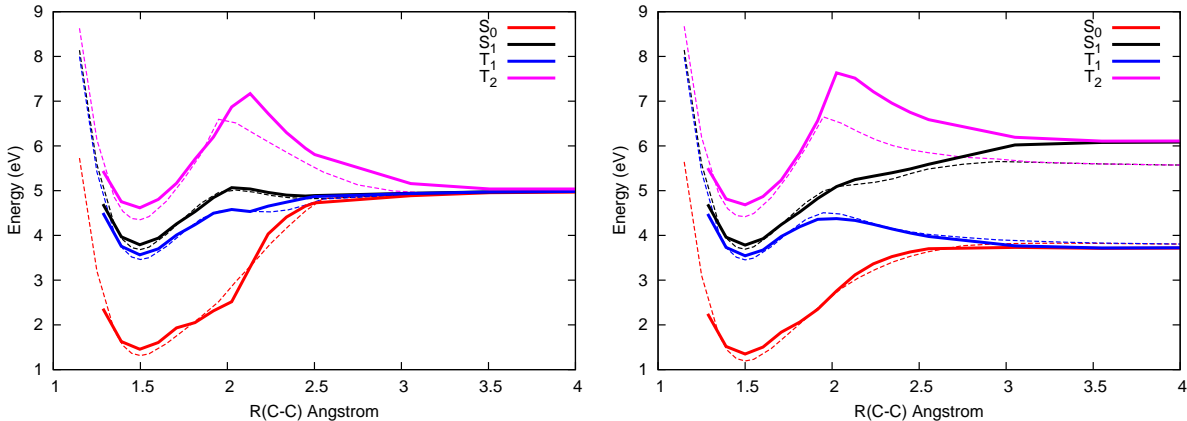|	R(C-O)	R(C-C)	∠CCO	θ^a
S_0 min.	1.225	1.510	121.3	0
S_1 min.	1.397	1.497	112.1	39.7
T_1 min.	1.377	1.500	112.3	40.1
T_2 min.	1.479	1.490	112.2	39.6
S_0/S_1 MXS	1.183	1.469/3.054	172.0/91.1	–
S_1/T_1 MXS	1.696	1.481	115.0	0
CH_3CO bent	1.177	1.504	128.1	–
CH_3CO linear	1.184	1.466	180.0	–

^{a} Out of plane CO bending angle.

Figure 1: Potential energy curves for the C-C dissociation of acetone. Thick lines, MRCI results. Dashed lines, semiempirical results. Left panel: S_1 optimized. Right panel: T_1 optimized. Energies are referred to the S_0 minimum. The semiempirical results are shifted along the R(C-C) axis by -0.05 Å.

than $h\nu_{max}$, because of the third power dependence of the emission intensity.

The S_0/S_1 and S_1/T_1 MXS shown here are similar in structure and energy to previous results [23, 24]. In particular, the S_1/T_1 MXS is found to have a C_{2v} symmetry with an elongated C-O bond, well above the S_1 minimum, in good agreement with Maeda et al. [24], although in their case the S_1/T_1 MXS was even higher in energy (see Table 1) with a longer C-O distance (1.794 Å). The S_0/S_1 MXS has instead a very stretched C-C bond, i.e. it approaches the ^2E Jahn-Teller conical intersection between the first two doublet states of the isolated acetyl radical.

In Figure 1 we show the potential energy curves along the C-C dissociation. The curves have been obtained performing SA-CAS geometry optimizations at fixed values of the R(C-C) coordinate, followed by MRCI calculations. The optimizations have been

conducted for the S_1 and T_1 states. Dissociation energies are shown in Table 1; our MRCI value for the ground state is 3.742 eV, that compares well with the experimental D_e value of 3.83 eV [29]. At large C-C distances the acetyl fragment has a bent equilibrium geometry in the ground state and a linear minimum in S_1, corresponding to the Jahn-Teller intersection of the acetyl radical mentioned above. At MRCI level, the conical intersection is 1.289 eV above the bent minimum in the ground state and 1.088 eV below the excited state at the same bent geometry. The potential energy curve for the dissociation in S_1 shows a very low barrier around R(C-C) = 2 Å, the top of which almost coincides with the dissociation energy, with a shallow minimum in between. No matter how accurate are these details, the S_1 and S_0 PES's get very close to each other beyond R(C-C) = 2.5 Å, and we shall see in section 4 that the nonadiabatic couplings cause fast $S_1 \rightarrow S_0$ transitions even at shorter distances. Therefore, a dissociation event starting in the S_1 PES will almost inevitably end up in S_0, with a bent acetyl radical. According to these considerations, it seems to be difficult to set a precise energy threshold for the dissociation in S_1.

The T_1 PES shows a barrier of about 0.634 eV from the dissociation limit, i.e. 4.376 eV above the S_0 minimum; using the ZPE values computed at semiempirical level (see next section) the transition state energy can be corrected to 4.21 eV, slightly higher than the triplet dissociation threshold evidenced by Haas et al. [8–10]. As apparent from Figure 1, the T_2 state undergoes an avoided crossing around R(C-C)=2 Å. In fact, in that region its description changes rather abruptly from $\pi \rightarrow \pi^*$ to $\sigma \rightarrow \pi^*$.

3 Reparameterization of the semiempirical Hamiltonian

In nonadiabatic molecular dynamics calculations, electronic energies and couplings are evaluated on the fly with a semiempirical Hamiltonian using the FOMO-CI method [38–40], in which CI wavefunctions are built with FOMOs, i.e. molecular orbitals obtained from an SCF with floating occupation numbers. In particular, the CI space considered was the same CAS space used in the ab initio calculations (5 electrons in 6 MO) and the Gaussian energy width of FOMOs was 0.1 Hartree. The standard set of AM1 parameters [41] was taken as a starting point for the reparameterization, using our ab initio MRCI data as targets. The method used for the determination of the improved set of semiempirical parameters is fully described in Ref. [40], here we only give a brief account. The reparameterization is based on the minimization of the function

$$F(\mathbf{P}) = \sum_i \left(\frac{V_i^{(T)} - V_i^{(S)}(\mathbf{P})}{V_i^{(T)}} \right)^2 W_i \tag{1}$$

where $\mathbf{P}$ is the set of semiempirical parameters, $V_i^{(T)}$ is a target quantity, $V_i^{(S)}$ is the corresponding FOMO-CI semiempirical value and W_i is a weight. For the search of the minimum of $F(\mathbf{P})$ we used the simplex algorithm combined with a simulated annealing procedure. In order to avoid the intrusion of orbitals representing the C-H bonds in the CI active space, we employed two different semiempirical β parameters for the hydrogen atoms (β_H^{SCF} and β_H^{CI}). The first one, β_H^{SCF}, set to a large negative value (-20 eV), was used to obtain the FOMOs. Then, the CI calculations yielding energies and wavefunctions were performed with β_H^{CI}, which value was optimized in the reparameterization procedure [40]. The full set of new semiempirical parameters is given in the supporting information.

In general, the FOMO-CI calculations gave a too low dissociation energy for the C-C bond on the S_0 PES. We decided therefore to shift all the semiempirical energies with the following additive function

$$U(r, \varphi) = p_1 \, \sigma(r|p_2, p_3) \, \sigma(\varphi|p_4, p_5) \qquad (2)$$

$$\sigma(x|x_m, \Delta x) = \begin{cases} 0 & \text{if } x \leq x_m - \Delta x/2 \\ -2\left(\frac{x-x_m}{\Delta x}\right)^3 + \frac{2}{3}\left(\frac{x-x_m}{\Delta x}\right) + \frac{1}{2} & \text{if } x - \Delta x/2 < x < x + \Delta x/2 \\ 1 & \text{if } x \geq x_m + \Delta x/2. \end{cases} \qquad (3)$$

were r is the larger of the two C-C bond lengths and φ is the value of the CCO bond angle relative to the shorter C-C bond. $\sigma(x|x_m, \Delta x)$ is a cubic sigmoid function going smoothly from 0 to 1 as x goes from $x_m - \Delta x/2$ to $x_m + \Delta x/2$. The parameters $p_1 \ldots p_5$ were determined after the semiempirical ones, in order to reproduce the correct dissociation energy for S_0 and T_1. In particular: $p_1 = 0.45$ eV, $p_2 = 3.3$ Å, $p_3 = 2.2$ Å, $p_4 = 155°$ and $p_5 = 40°$. The additive term $U(r, \varphi)$ is not evaluated if both the C-C bonds are larger than $p_2 - p_3/2$. However, this never happens during the dynamics (and our FOMO-CI active space is not tuned to provide a good description in that case).

In Tables 3 and 4 we show the energetic and geometrical parameters considered in the optimization. The semiempirical results reported include the effect of the added potential $U(r, \varphi)$. To keep our data set as consistent as possible, all the target values were taken from our MRCI calculations. Together with S_0, S_1 and T_1 equilibrium structures for the reactant and products, we considered also some points along the C-C dissociation path on S_1. In particular, the point at R(C-C)=2.026 Å, corresponding to the outer maximum on the S_1 MRCI curve (see Figure 1, left panel), was obtained at the semiempirical level as a true transition state. Note that there is also an outer shallow minimum on the S_1 PES, so that the barrier energy is very close to the S_1 dissociation energy (see Table 3). As one can see from Table 4, the C-C bond lengths of the S_0, S_1 and T_1 minima at semiempirical level are about 0.05 Å longer than the corresponding target values. The same holds for the longer C-C bond at the S_1 saddle point; combined with the slope of the S_0 PES, this makes so that the ground to excited state energy differences computed semiempirically at this geometry are smaller than the target values by 0.4–0.7 eV. To facilitate a visual comparison with the ab initio potential energy curves in Figure 1, the semiempirical ones have been shifted by -0.05 Å on the R(C-C) axis. The semiempirical entries of Table 3 concerning the excited states are in very good agreement with the MRCI ones (the largest differences amount to 0.18 eV for T_2 in its high energy region and 0.11 eV for the other states).

The two MXS optimized at SA-CAS level were not considered in the reparameterization for practical reasons; of course their correct characterization is important for the dynamics. With the semiempirical FOMO-CI calculations we found the S_0/S_1 MXS to be 4.857 eV above the ground state minimum, with the two R(C-C) equal to 2.526 and 1.490 Å, R(C-O) = 1.196 Å and the $\angle$OCC = 159.4° for the acetyl moiety. These results are in good agreement with the ab initio ones (see Table 2). The C_{2v} S_1/T_1 MXS is 5.263 eV above the ground state, with R(C-C) = 1.500 Å and an elongated R(C-O) = 1.677 Å. In this case the semiempirical results give a too high MXS (about 0.4 eV above the MRCI data). Note however that: a) there is a large energy difference between SA-CAS and MRCI results; b) at semiempirical level, S_1 and T_1 stay close in energy in a large interval of C-O bond lengths around the MXS point: for example, with R(C-O) = 1.577 Å, the T_1 energy decreases by 0.63 eV and the S_1-T_1 energy difference is still as low as 0.05 eV; c) the semiempirical FOMO-CI result is close to the CASPT2 data of ref. [24].

7

Table 3: Energy MRCI target values (eV) and corresponding semiempirical results obtained with the reparameterized Hamiltonian. The single state energies are referred to the S_0 minimum, while the energy differences between two states are vertical transition energies.

geometry	quantity	target	semiemp.	difference	weight
S_0 min.	$E(S_1) - E(S_0)$	4.498	4.481	0.017	0.20
	$E(T_1) - E(S_0)$	4.168	4.181	-0.013	0.20
	$E(T_2) - E(S_0)$	6.080	5.927	0.153	0.20
S_1 min.	$E(S_1)$	3.792	3.682	0.110	1.50
	$E(S_1) - E(S_0)$	2.336	2.371	-0.035	0.70
	$E(T_1) - E(S_0)$	2.111	2.151	-0.040	0.70
	$E(T_2) - E(S_0)$	3.161	3.037	0.124	0.70
T_1 min.	$E(T_1)$	3.543	3.454	0.089	0.00
	$E(S_1) - E(S_0)$	2.434	2.498	-0.064	0.50
	$E(T_1) - E(S_0)$	2.195	2.261	-0.066	0.50
	$E(T_2) - E(S_0)$	3.335	3.226	0.109	0.50
S_0 diss.	$E(S_0)$	3.742	3.793	-0.051	1.50
S_1 diss.	$E(S_1)$	5.031	5.024	0.007	1.50
S_1 at R(C-C)=1.920	$E(S_1)$	4.846	4.782	0.064	1.20
	$E(S_1) - E(S_0)$	2.533	2.532	0.001	1.00
	$E(T_1) - E(S_0)$	2.183	2.169	0.014	1.00
	$E(T_2) - E(S_0)$	3.887	3.703	0.184	0.20
S_1 at R(C-C)=2.026[a]	$E(S_1)$	5.067	5.015	0.052	1.50
	$E(S_1) - E(S_0)$	2.550	2.122	0.428	0.20
	$E(T_1) - E(S_0)$	2.063	1.678	0.385	0.20
	$E(T_2) - E(S_0)$	4.353	3.648	0.705	0.20
S_1 at R(C-C)=2.502	$E(S_1)$	4.891	4.823	0.068	1.80
	$E(S_1) - E(S_0)$	0.163	0.265	-0.102	0.10
	$E(T_1) - E(S_0)$	0.141	0.126	0.015	0.10
	$E(T_2) - E(S_0)$	1.078	1.060	0.018	0.10

[a]Semiempirical values refer to the S_1 transition state optimization, resulting in R(C-C)=2.083 Å.

Table 4: Geometrical target parameters (from SA-CAS optimizations) and corresponding semiempirical results obtained with the reparameterized Hamiltonian. Distances in Å, angles in degrees.

geometry	quantity	target	semiemp.	weight
S_0 min.	R(C-O)	1.225	1.231	2.60
	R(C-C)	1.510	1.549	2.60
	∠OCC	121.3	122.2	0.50
S_1 min.	R(C-O)	1.397	1.373	2.40
	R(C-C)	1.497	1.545	2.00
	∠OCC	112.1	113.7	1.00
	O-C-C-C	140.5	142.8	0.50
T_1 min.	R(C-O)	1.377	1.355	1.20
	R(C-C)	1.500	1.552	1.20
	∠OCC	112.3	113.9	0.60
	O-C-C-C	139.6	142.3	0.50
S_0 diss.	R(C-O)	1.177	1.199	1.00
	R(C-C)	1.504	1.513	1.00
	∠OCC	128.1	135.3	0.20
S_1 diss.	R(C-O)	1.184	1.183	0.50
	R(C-C)	1.466	1.482	0.50
S_1 at R(C-C)=2.026[a]	R(C-C)	2.026	2.083	1.00
	∠OCC[b]	124.5	138.0	0.10
	∠OCC[c]	106.1	103.3	0.20
	O-C-C-C	127.0	117.8	0.40
	H-C-H-H[d]	133.1	135.2	0.80
S_1 at R(C-C)=2.502	H-C-H-H[d]	145.6	146.6	0.10

[a]Semiempirical values refer to the S_1 transition state optimization. [b]Bond angle defined with the shortest C-C bond. [c]Bond angle defined with the longest C-C bond. [d]Dihedral angle evaluated for the dissociating CH_3 group.
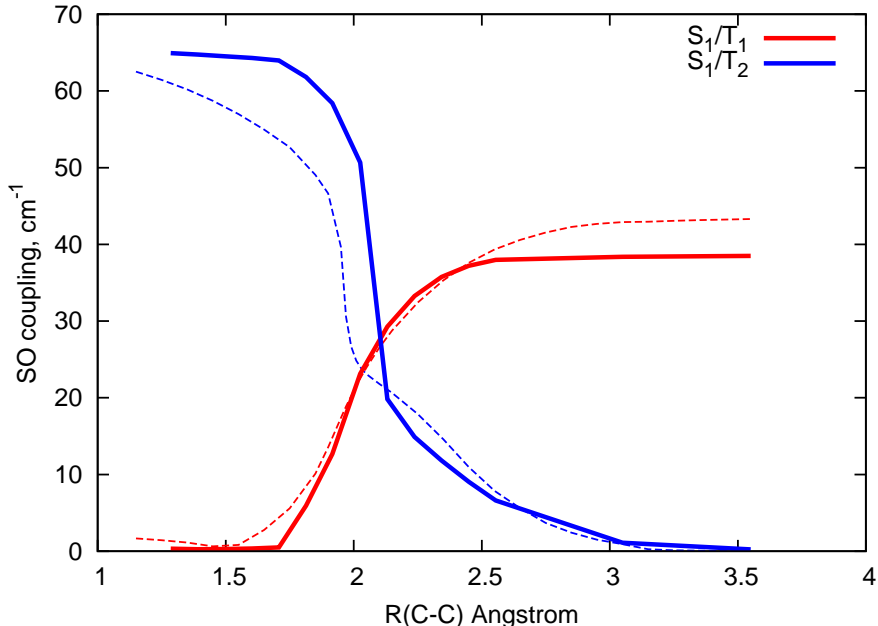
Figure 2: Absolute value (see text) of the spin-orbit coupling at T_1 optimized geometries. Thick lines: SA-CAS results. Dashed lines: semiempirical results. Red lines: S_1/T_1 coupling. Blue lines: S_1/T_2 couplings. To be consistent with Figure 1, the semiempirical results are shifted on the R(C-C) axis by -0.05 Å.

Overall, the agreement between the MRCI calculations and the semiempirical FOMO-CI is very good. In particular, the curves shown in Figure 1 are reproduced with an accuracy at least semiquantitative, with the largest discrepancies for the T_2 state and the dissociation energy of S_1 (but only at the T_1 optimized geometry). Note that, if executed on a single CPU, one of the MRCI calculations we performed required a computing time about 10^7 times longer than a semiempirical FOMO-CI one.

The SO couplings have been obtained at semiempirical level with a one electron effective Hamiltonian [42] containing the atomic parameters ξ_N and ξ_C. These parameters were fitted to ab initio target data evaluated with the nonrelativistic SA-CAS wavefunctions and the full Breit-Pauli Hamiltonian (using the GAMESS program package [43]). In particular, we considered the S_1/T_1 and S_1/T_2 SO couplings along the T_1 C-C dissociation curve (i.e. at the same set of geometries used to obtain the right panel of Figure 1). The absolute value of the singlet/triplet SO coupling, defined as $\sqrt{\sum_m \left| \left\langle S \left| \hat{\mathcal{H}}_{SO} \right| T_m \right\rangle \right|^2}$ (where $\hat{\mathcal{H}}_{SO}$ is the SO Hamiltonian and T_m is one of the three component of the triplet state) is shown in Figure 2. The fitting of the SO semiempirical parameters was performed after the reparameterization discussed above; we obtained $\xi_C = 138$ and $\xi_N = 92$ cm^{-1}. The behavior of the ab initio couplings is nicely reproduced with the FOMO-CI semiempirical calculations; note that, as expected, the S_1/T_1 SO interaction is vanishingly small at short C-C distances.

4   Photodissociation dynamics

The simulations of the acetone nonadiabatic dynamics after $n \rightarrow \pi^*$ photoexcitation have been performed with the surface hopping scheme developed in our group [42, 44, 45], with

PESs and couplings evaluated on-the-fly in the FOMO-CI semiempirical framework. Both spin-orbit and dynamical couplings have been accounted for within the "spin-adiabatic" approach [42, 45]. The SO coupled Hamiltonian is diagonalized in the subspace of the four spin unmixed ("spin-diabatic") states S_0, S_1, T_1 and T_2, producing 8 dynamically coupled spin-adiabatic PES where the nuclear trajectories are propagated. The numerical integration of the electronic time dependent Schrödinger equation (TDSE) takes advantage of our local diabatization procedure, which has proven to be inherently stable even in the presence of very weakly avoided crossings [44, 46]. This allowed us to perform the integration of the electronic TDSE with the same time step used for the propagation of Newton's equations of motion for the nuclei ($\Delta t = 0.1$ fs). A decoherence correction as described in ref. [47] was applied, with the C parameter set to 0.1 Hartree.

The starting conditions were sampled from the ground state Wigner distribution, based on the S_0 normal modes, weighted with the electric dipole radiative transition probability to the spin-adiabatic states in the excitation energy range $\Delta E_{exc} = 3.8$–5.1 eV. We note that the Wigner sampling for a given vibrational state yields a distribution of energies that averages to the appropriate quantum level. The six normal modes corresponding to C-H stretchings were kept frozen in the sampling procedure, in an attempt to partly amend for the problems connected with the ZPE leakage in classical trajectories. The two low frequency modes, corresponding to the internal rotations of the methyl groups, were also treated in a special way: in particular, the coordinate sampling was frozen along these modes, while regularly performing the momentum sampling. In fact, for such low frequency modes (126 and 158 cm^{-1} according to the harmonic normal mode treatment, to be compared with the experimental values of 77 and 125 cm^{-1} [48]) the sampled normal mode displacements can be so big as to cause problems connected with anharmonicity and spurious mixing with other modes, especially the C-H stretchings. Rather, three different orientations of the methyl groups, corresponding to
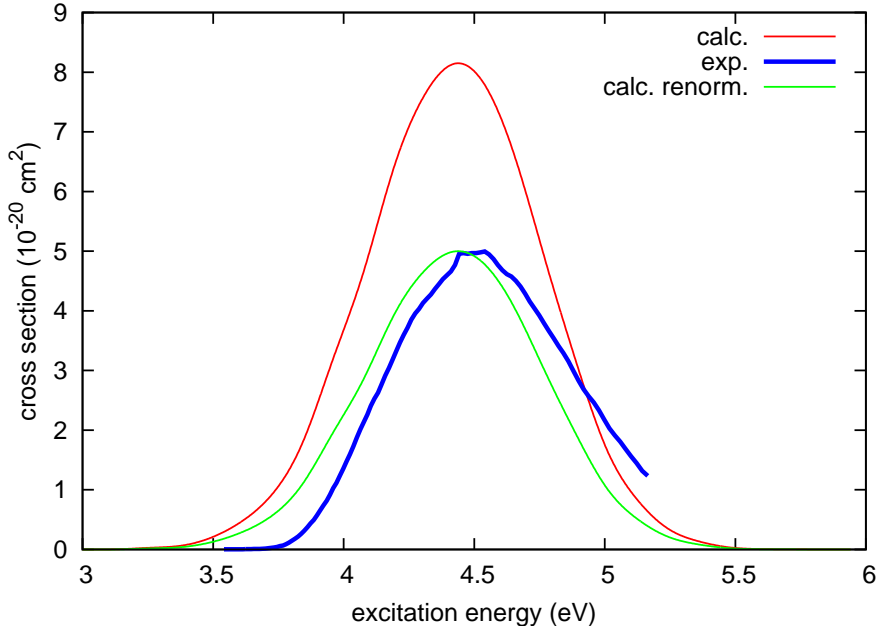

Figure 3: Acetone absorption spectrum, $n \rightarrow \pi^*$ transition. Red line: present calculations. Thick blue line: experimental data [35]. Green line: present calculations, renormalized to match the experimental maximum cross section.

stationary points of the S_0 PES, were considered in the sampling: eclipsed-eclipsed (the C_{2v} minimum), eclipsed-staggered and staggered-staggered [48]. Each one of the three configurations was weighted in the sampling by a Boltzmann factor, evaluated using the MP2 relative energies of Smeyers et al [48].

All the trajectories started on the fifth spin-adiabatic state, practically corresponding to S_1. The acetone absorption spectrum, obtained as a by-product of the sampling procedure, is shown in Figure 3. The agreement with the experimental data is reasonably good, expecially considering that the transition dipole moment was not taken into account in the reparameterization procedure. We evaluate that the semiempirically computed transition dipole is overestimated by an average factor of 1.28.

A total of 1140 trajectories were run; 98 of them were discarded because of unrecoverable errors in the integration of the equations of motion. Hence, 1042 good trajectories were retained for the final analysis. For each trajectory the following stop conditions were imposed: a) maximum propagation time of 50 ps; b) one of the two C-C bond longer than 4.76 Å(9.0 bohr); c) running on S_0 during more than 0.5 ps. The last condition was introduced because the dissociation lifetime in the ground state potential well is estimated to be much longer than 50 ps.

In figure 4 we show the distribution of the excitation energies with respect to the total energy of each trajectory (referred to the S_0 minimum). The starting kinetic energy, averaged over the full swarm of trajectories, evaluates to 0.61 eV, in line with the result
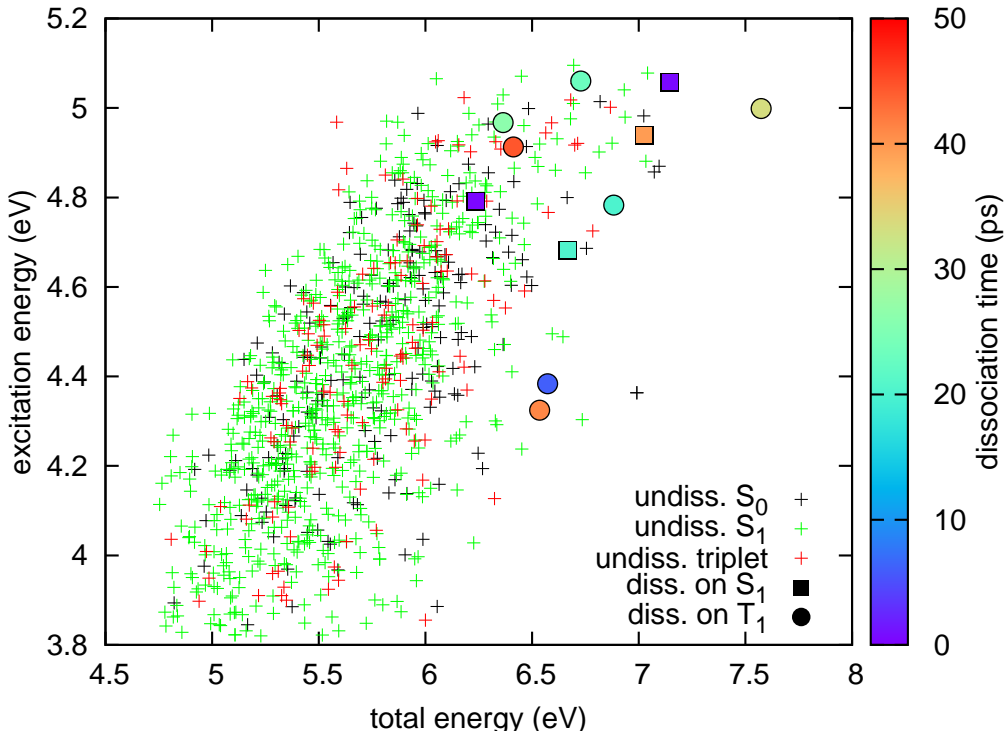

Figure 4: Excitation energy versus total energy after excitation (eV). Crosses: trajectories not showing dissociation within the first 50 ps and ending the simulation on S_0 (black), S_1 (green), or a triplet state (red). Colored squares (circles): trajectories dissociating on a singlet (respectively, triplet) PES. Colors of the filled symbols are used, in a rainbow scheme, to represent dissociation times, arbitrarily set as the time needed for one of the two C-C bond to reach 4.23 Å (8.0 bohr). Total energies are referred to the S_0 minimum.

12

for the harmonic ZPE of S_0 (1.24 eV, excluding the C-H stretchings). A similar value of 0.66 eV is obtained for the averaged potential energy on the S_0 PES. Black and red crosses represent trajectories running on S_0 and T_1, respectively, that have not undergone dissociation after 50 ps. Filled symbols are used to represent the 11 trajectories (1.1 %) undergoing dissociation of one C-C bond within 50 ps. The dissociation time t_{diss} shown by the color palette is arbitrarily set as the time needed for one of the two C-C bond lengths to reach 4.23 Å (8.0 bohr). Due to the 50 ps time limitation, we are only able to see dissociation from some of the most energetic trajectories, belonging to the upper right corner of figure 4. The C-C bond breaking takes place either on the T_1 (7 trajectories) or on the S_1 PES (4 trajectories). In the latter case all 4 trajectories hop to the ground state at distances between 2.71 and 3.14 Å, i.e. in the region where the almost isolated acetyl radical exhibits its typical Jahn-Teller intersection (see section 2). According to the present results, the average t_{diss} of acetone after $n \to \pi^*$ excitation appears to be much longer than 50 ps. Note that we are not taking into account the possibility of dissociation after the system has reverted back to the ground state, which is probably an even slower process.

Since the SO interactions in acetone are weak at all geometries, the analysis of the simulation results is better performed in terms of spin-diabatic singlet and triplet states. In Figure 5 we show the populations $\bar{p}_K$ of the spin-diabatic states. They are obtained by averaging over the full swarm of trajectories the quantities

$$p_K(t) = \sum_{m_K} |\langle K, m_K | \psi \rangle_t|^2 , \qquad (4)$$

where $|\psi\rangle$ is the spin-adiabatic state on which the given trajectory is running at the given time t, and $|K, m_K\rangle$ are the spin-diabatic states (m_K enumerating the components of the spin multiplet K). Immediately after the excitation, the nuclear trajectories start to oscillate around the S_1 equilibrium geometry, which differs from the ground state one mainly in that the R(C-O) distance is longer and the central C atom is pyramidalized (see
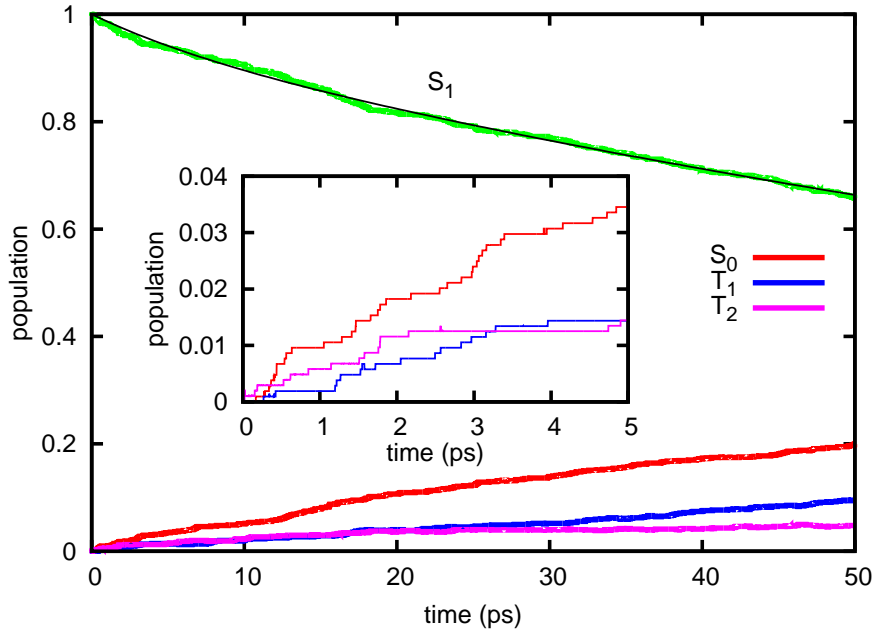

Figure 5: Populations of the spin-diabatic states. The black line is a biexponential fit of $\bar{p}_{S_1}$ (see text).

Table 4). Almost nothing else happens during the first 200 fs (see the inset of Figure 5), in agreement with the ab initio Full Multiple Spawning results of Sølling and coworkers [6] (only the singlet states were taken into account in their simulation). In particular, during that time only 1 trajectory (out of 1042) decayed to the ground state, while 3 trajectories show a hop to T_2.

The S_1 lifetime can be obtained from the final population at 50 ps by assuming an exponential decay:

$$\tau_{S_1} \text{ (ps)} = -50/ln(\bar{p}_{S_1}) \tag{5}$$

Taking into account all trajectories we get $\tau_{S_1} = 121$ ps, i.e. a decay rate of 8.3 ns^{-1}, which is the sum of the IC and ISC contributions. Since all the trajectories hopping to T_2 are expected to end up in T_1 in a relatively short time (see the discussion below in this section), when considering the ISC process we shall lump together the two triplet states. From the final S_0, T_1 and T_2 populations we get the IC and ISC rate constants $K_{IC} = 4.8$ ns^{-1} and $K_{ISC} = 3.5$ ns^{-1}.

A more refined representation of the S_1 decay is obtained by fitting $\bar{p}_{S_1}(t)$ with a biexponential function:

$$p(t) = W_1 e^{-t/\tau_1} + (1 - W_1)e^{-t/\tau_2}. \tag{6}$$

In this way we get a fast decay time $\tau_1(S_1) = 8.1$ ps with a very low weight $W_1 = 0.06$ and a more important slow component $\tau_2(S_1) = 142$ ps (fitting with a single exponential would yield $\tau_{S_1} = 114$ ps).

We also evaluate the triplet quantum yield from the situation at 50 ps, as

$$\Phi_{ISC} = \frac{\text{n. of trajectories in } T_1 \text{ or } T_2}{\text{n. of trajectories having undergone IC, ISC or direct dissociation in the } S_1 \text{ PES}} \tag{7}$$

The denominator accounts for all the decay channels that allow to quit the S_1 potential well. For the whole swarm of trajectories we find $\Phi_{ISC} = 0.42$, well in the midst of the λ_{exc} dependent experimental values [18–20].

Our computed lifetimes are compatible with the upper limit of 10 ns set by Haas and coworkers [8–10] on the fast S_1 decay component τ_{fast}. However, since some experimental evidence indicates that the S_1 lifetime should be considerably longer that 100 ps with ΔE_{exc} between 4.0 and 4.9 eV [4, 5, 7], our IC and ISC rates are probably somewhat overestimated. A source of error in this context may be the ZPE leakage, i.e. the fact that ZPE can be freely exchanged among vibrational modes in classical trajectories, possibly facilitating nonradiative decay processes on a timescale much longer of the relevant vibrational periods. Also, the Wigner sampling of initial conditions in the ground state yields a distribution of energies, instead of a single level; after vertical excitation with a given value of ΔE_{exc}, we get a fraction of trajectories with unduly high total energies E_{tot}, that may undergo a faster decay (and also, of course, a fraction of less energetic trajectories that decay more slowly). Finally, any evaluation based only on the first 50 ps after excitation is likely to overestimate the decay rate that would be found with longer simulations. In fact, our biexponential fit yields a slow component (the only one that counts in the long term) with $\tau_2 = 142$ ps, about 20% longer than the value obtained by eq. (5) with a single exponential fit.

In order to highlight the dependence of the IC and ISC rates on ΔE_{exc} and E_{tot}, we show in Table 5 the results obtained for subsets of trajectories falling into selected ranges

Table 5: Number of trajectories in the ground and triplet states at the end of the run (50 ps) for selected ranges of excitation or total energies (ΔE_{exc} and E_{tot}, respectively). S_1 lifetimes τ_{S_1} and triplet quantum yields Φ_{ISC}, computed according to eqs. (5) and (7).

ΔE_{exc} range (eV)	n. of trajs.	trajs. in S_0	trajs. in T_1 or T_2	τ_{S_1} (ps)	Φ_{ISC}
$3.80 - 3.90$	36	4 (11%)	3 (8%)	231	0.43
$3.90 - 4.00$	53	3 (6%)	9 (17%)	195	0.75
$4.00 - 4.20$	176	31 (18%)	17 (10%)	157	0.35
$4.20 - 4.40$	249	45 (18%)	34 (14%)	131	0.43
$4.40 - 4.60$	238	50 (21%)	37 (16%)	110	0.43
$4.60 - 4.80$	185	53 (29%)	26 (14%)	90	0.32
$4.80 - 5.10$	105	18 (17%)	23 (22%)	101	0.53
$3.80 - 5.10$	1042	204 (20%)	149 (14%)	121	0.42
E_{tot} range (eV)	n. of trajs.	trajs. in S_0	trajs. in T_1 or T_2	τ_{S_1} (ps)	Φ_{ISC}
$4.70 - 4.90$	26	1 (4%)	1 (4%)	625	0.50
$4.90 - 5.10$	61	6 (10%)	4 (7%)	279	0.40
$5.10 - 5.30$	131	19 (14%)	13 (10%)	179	0.41
$5.30 - 5.60$	258	43 (17%)	39 (15%)	131	0.48
$5.60 - 5.90$	255	48 (19%)	34 (13%)	129	0.41
$5.90 - 6.20$	194	57 (29%)	32 (16%)	81	0.36
$6.20 - 6.60$	84	22 (26%)	17 (20%)	80	0.42
$6.60 - 7.60$	33	8 (24%)	9 (27%)	69	0.45
$4.70 - 7.60$	1042	204 (20%)	149 (14%)	121	0.42

of these two variables. We find that τ_{S_1} increases towards the lowest end of the ΔE_{exc} range, and even more sharply if we consider E_{tot}. This is in qualitative agreement with Haas' observation that the fast decay of S_1 is absent near the origin of the absorption band [8–10], but of course a trajectory based treatment cannot reproduce the state specific behavior that characterizes the very first vibrational levels in S_1. Up to $\Delta E_{exc} \simeq 4.8$ eV we see that the IC rate increases faster than the ISC one as a function of ΔE_{exc}; the same holds if we consider the dependence on E_{tot}, up to ~ 6.2 eV. This is expected because the dynamic or derivative couplings, contrary to the SO ones, depend on the nuclear velocities. As a result, the triplet quantum yield Φ_{ISC} decreases with energy (either ΔE_{exc} or E_{tot}), but not so sharply as required by the kinetic models previously elaborated to explain the photodissociation data [18, 19].

The slow decay component τ_{slow} found by Haas and coworkers [8–10] in the μs range is of course quite outside the span of our simulation. Such a lifetime can only pertain to the T_1 state, and in fact it decreases sharply at the onset of dissociation on T_1 ($\Delta E_{exc} = 4.052$ eV). We are then led to postulate that S_1 is kept populated by backward $T_1 \rightarrow S_1$ transitions and τ_{slow} essentially coincides with the lifetime of T_1 (see scheme in Fig. 6). In our simulation we observed only one $T_1 \rightarrow S_1$ hop, out of 150 trajectories that reached a triplet state. Unlike standard cases of E-type delayed fluorescence [49], the most reliable experiments performed on acetone exploited collisionless conditions [9], so the S_1/T_1 equilibrium ratio would obey microcanonical statistics. The density of states in the T_1 PES was evaluated to be 80 per cm^{-1} at the energy corresponding to the lowest vibrational level in S_1; therefore, the equilibrium population ratio $R(S_1/T_1)$ is probably very small. $R(S_1/T_1)$ is related to the $T_1 \rightarrow S_1$ transition rate constant K_{invISC}:

$$R(S_1/T_1) = \frac{K_{invISC}}{K_{ISC}} \tag{8}$$

Therefore, K_{invISC} is also small and it is quite reasonable to find very few $T_1 \rightarrow S_1$ hops in the first 50 ps. At energies below the T_1 dissociation threshold, we suggest that the irreversible decay of both S_1 and T_1 in the μs range is due at least in part to the $S_1 \rightarrow S_0$ IC, which is slow because of the small S_1 population. However, we have no data to exclude a contribution from the $T_1 \rightarrow S_0$ ISC in the same time scale. The fluorescence decay times τ_{slow} measured in supersonic beams [9] are longer for $(CD_3)_2CO$ than for $(CH_3)_2CO$, in agreement with the prediction of a smaller $R(S_1/T_1)$ ratio for the deuterated compound, due to its larger T_1 density of states.

We also computed the fluorescence emission rate as a function of time (see Figure S1 in the supporting informations and ref. [50] for the relevant equations). We found an almost perfectly exponential decay, except at the very beginning (2–3 ps), where coherent oscillations of the swarm of trajectories cause large changes in the emission rate. The fluorescence lifetime turns out to be 111 ps, very close to the value of 114 ps obtained by fitting the S_1 population decay by a single exponential. The exponential prefactor, i.e. the fluorescence rate constant, is $K_F = 0.58$ μs^{-1}. By computing the $S_1 - S_0$ transition dipoles and energy differences at 150000 geometries, sampled according to the normal coordinate distribution for the lowest vibrational level in S_1, we got almost the same value, $K_F = 0.66$ μs^{-1}. Taking into account that the semiempirical FOMO-CI method overestimates the $S_0 - S_1$ transition dipole by a factor 1.28 (see above), we can correct the computed K_F value and obtain $K_F = 0.36$ μs^{-1}, in very good agreement with the estimate of Szilágyi et al. [20]. Gas phase measurements of the fluorescence quantum yield at room temperature [22] show that Φ_F increases with the excitation wavelength, from $2.5 \cdot 10^{-4}$ at $\lambda_{exc} = 248$ nm ($\Delta E_{exc} = 5.00$ eV), to $7.1 \cdot 10^{-4}$ at 308 nm (4.03 eV).

16

Assuming $\Phi_F = K_F \, \tau_{S_1}$, these values would correspond to lifetimes ranging from 0.7 to 1.9 ns. Of course the fluorescence measured in steady state conditions is emitted during both the fast initial decay and the slow one (with a smaller S_1 population), so the above lifetimes are intermediate between τ_{fast} and τ_{slow}.

A more detailed analysis of the decay mechanism can be obtained from Table 6, where we list some of the relevant structural and energetic variables at the time of surface hops, averaged over all trajectories and over the whole duration of the simulation (50 ps). The elongation of the C-O bond causes the four states to get closer in energy; it may therefore trigger non radiative transitions from S_1. This appears to be the case for the hops to T_2, which occur with an average R(C-O) of 1.428 ± 0.071 Å, considerably longer than the equilibrium bond length of 1.373 Å in S_1. Apparently this effect is not so important for the $S_1 \rightarrow T_1$ transitions; note that the SO coupling between the two spin-diabatic states, already very weak around the minimum of the S_1 state (~ 1 cm^{-1}) is further reduced when stretching the C-O bond, thus approaching the S_1/T_1 MXS region (the SO coupling vanishes at the C_{2v} geometry of the MXS for symmetry reasons [45]). On the contrary, the S_1/T_2 SO coupling is larger (around 60 cm^{-1}, see Figure 2) and not much affected by the C-O distance. As one may appreciate from Table 6, the larger coupling compensates for the larger energy difference, so that the T_2 state has a non negligible influence on the overall ISC rate: the number of $S_1 \rightarrow T_2$ transitions is in fact close to that of $S_1 \rightarrow T_1$ hops. The fate of the trajectories running on the T_2 PES is to decay to T_1, and in the first 50 ps there is a fast interchange of population between the triplet states, with 43
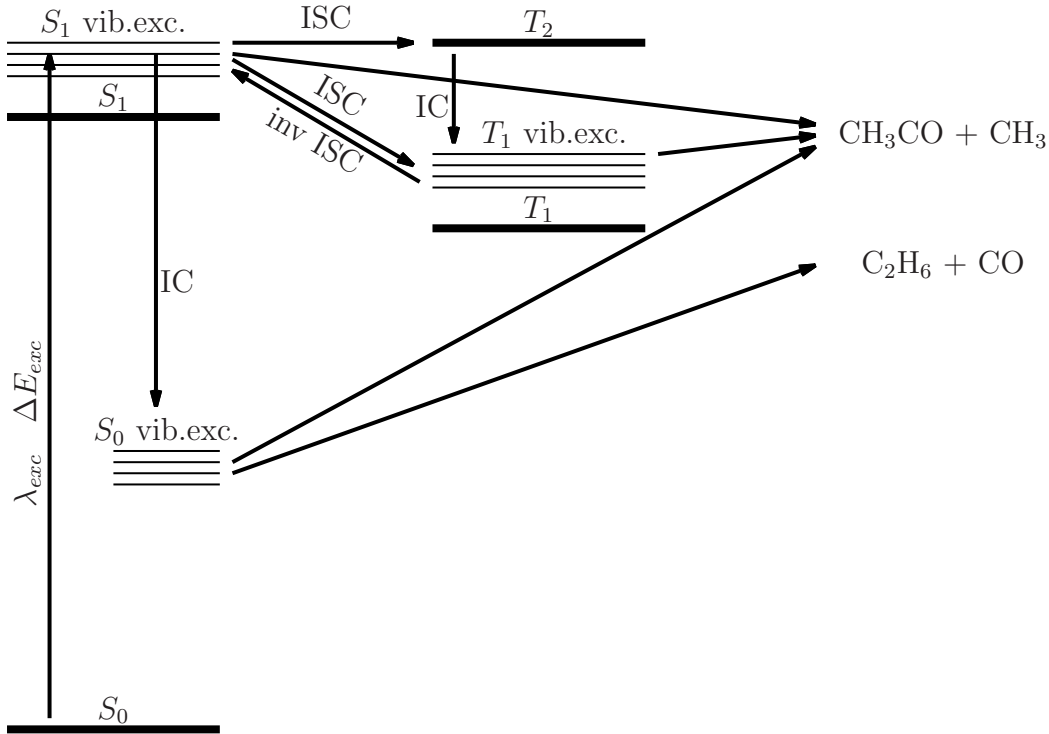

Figure 6: Scheme of the excited state decay and photodissociation of acetone. For the isolated molecule, all processes are isoenergetic with the exception of initial excitation. For graphical convenience, we depicted some energy levels (vibrationally excited S_0 and T_1, and the reaction products) at different energies, roughly corresponding to their average potential energy.

Table 6: Nonadiabatic transitions between spin-diabatic states: number and averaged dynamical quantities. Distances in Å, angles in degrees, energies in eV.

transition	$S_1 \to T_1$	$S_1 \to T_2$	$S_1 \to S_0$	$T_2 \to T_1^a$
number	81 (7.8%)	69 (6.6%)	214 (20.5%)	38 (3.6%)
R(C-O)	1.381 ± 0.044	1.428 ± 0.071	1.369 ± 0.062	1.478 ± 0.064
O-C-C-C	140.9 ± 11.7	141.9 ± 13.4	142.2 ± 12.5	133.7 ± 8.2
R(C-C)$_{max}$	1.592 ± 0.039	1.587 ± 0.043	1.620 ± 0.182	1.568 ± 0.033
R(C-C)$_{min}$	1.536 ± 0.037	1.530 ± 0.031	1.527 ± 0.045	1.521 ± 0.035
ΔE^b	0.222 ± 0.034	-0.519 ± 0.159	2.368 ± 0.619	0.533 ± 0.174
E_{tot}^c	5.752 ± 0.513	5.873 ± 0.400	5.822 ± 0.453	6.005 ± 0.406
E_{kin}^d	1.312 ± 0.339	0.761 ± 0.260	2.980 ± 0.619	1.308 ± 0.303

[a]Only the last transition of this kind is considered. In the other cases, only one transition of the given kind per trajectory was present in the simulations. [b]Energy difference between the two spin-diabatic states involved. [c]Total energy, referred to the ground state minimum. [d]Nuclear kinetic energy.

$T_2 \to T_1$ and 25 $T_1 \to T_2$ hops. Since these transitions are due to the dynamic coupling, the averaged kinetic energy at the $T_2 \to T_1$ hops is larger than at the $S_1 \to T_2$ ones, even if T_2 is higher lying than S_1. The $S_1 \to S_0$ transitions occur with quite a high energy difference between the two states (the average value is 2.368 eV). The S_0/S_1 MXS referred to in section 3 is therefore not involved. No transitions from the triplet states to S_0 are obtained within 50 ps.

In summary, we propose that three photodissociation mechanisms can be active, depending on the excitation wavelength, as schematized in Fig. 6: (A) ground state dissociation, after $S_1 \to S_0$ IC or possibly also through $S_1 \to T_1 \to S_0$ ISC, to produce either $CH_3CO + CH_3$ or $C_2H_6 + CO$ [21]; (B) T_1 dissociation, particularly fast over $\Delta E_{exc} \simeq 4.05$ eV; and, (C) S_1 dissociation, at higher energies, with the possibility of IC to S_0 along the dissociation pathway, which might put the threshold to enter this channel at energies lower than the pure S_1 dissociation would require. In principle, there should be no clear cut distinction between mechanisms (A) and (C), the difference being quantitative rather than qualitative: in the former case the radiationless transition that populates S_0 takes place at geometries not so far from the equilibrium ones for the involved states, while in the latter it occurs when the dissociation in S_1 is well under way or almost accomplished. However, all the 214 trajectories analyzed in Table 6 under the heading $S_1 \to S_0$ clearly belong to mechanism (A), the hops never taking place with R(C-C) > 1.8 Å, while the 4 that dissociate in S_1, i.e. with mechanism (C), do hop at R(C-C) > 2.7 Å, without intermediate cases.

The mechanisms discussed above have been already considered in the literature [2–26], and have been put at the basis of complex kinetic models. However, we think that the interpretation of experiments performed in gas phase, where the effects of collisions cannot be neglected, is quite hard and still not satisfactory as to the consideration of various forms of quenching and of the $S_1 \to S_0$ IC. When the molecule is in the S_1 state, collisional quenching can be electronic or vibrational: the former does shorten the S_1

lifetime, whereas the latter has the opposite effect, because the ISC rate and even more the IC one are smaller at lower vibrational energies (as confirmed by the increase of the gas phase fluorescence quantum yield with the pressure of the buffer gas [22]). In T_1, electronic quenching by closed shell atoms or molecules can be excluded (but not if the quencher is O_2), while vibrational quenching can trap acetone in the potential well; in this case, both dissociation in the T_1 surface and ISC to S_1 would become temperature dependent activated processes. Finally, the ground state dissociation time is probably much longer than in the excited states, because of the deeper potential well, so the vibrational quenching can be more effective and lead to irreversible stabilization of the molecule. It is then clear that careful consideration of all these distinct forms of quenching and of their effects is mandatory in setting up photophysical models of gas phase acetone photochemistry.

5   Conclusions

We performed on the fly surface hopping simulations of the dynamics of photoexcited acetone in the $n \to \pi^*$ band. Four spin diabatic states (S_0, S_1, T_1 and T_2) were considered; the spin-orbit and dynamic couplings were concurrently taken into account. The trajectories were run up to 50 ps, which is a time long enough to evaluate the transition rates and to allow for just a few dissociation events. Internal Conversion (IC) to S_0 and InterSystem Crossing (ISC) to T_1 or T_2 take place at comparable rates; T_2 eventually will decay to T_1 by IC, and this route accounts for almost half of the total triplet population. This shows that the simultaneous treatment of spin-orbit and dynamic couplings and the inclusion of T_2 are mandatory features of a realistic simulation of the $n \to \pi^*$ photodynamics of acetone.

Taking into account our results, as well as experimental evidence from various sources [2–12,14–21], we propose the following S_1 decay mechanism for the isolated molecule. The first step is IC to S_0 or ISC to T_1, the two decay channels being of approximately the same importance. We estimate the associated lifetime of S_1, τ_{fast}, to be in the range 90–130 ps, at medium excitation energies in the $n \to \pi^*$ band, i.e. between 4.2 and 4.8 eV. These values of τ_{fast} are in the right order of magnitude but probably somewhat underestimated, since experimental evidence has been interpreted to imply longer lifetimes [4,5,7]. We find that the τ_{fast} lifetime increases sharply at the lower energy end of the $n \to \pi^*$ band, in agreement with other experimental observations [8–10]. After the fast decay, S_1 remains populated for a much longer time, corresponding to the lifetime of T_1, because of upward $T_1 \to S_1$ ISC. The S_1/T_1 population ratio being small, the irreversible $S_1 \to S_0$ IC is a slow process by which the overall population of the two excited states can leak out, with a lifetime τ_{slow} of the order of microseconds [8–10]. At excitation energies higher than the barrier in the T_1 surface (4.05 eV) the C-C bond dissociation in this state becomes much faster and the decay mechanism through S_1 is then less important. At low energies, a contribution of the $T_1 \to S_0$ ISC to the decay rate cannot be excluded.

Three channels are open for the Norrish type-I C-C bond cleavage of acetone: dissociation in the ground state, after $S_1 \to S_0$ IC or possibly $S_1 \to T_1 \to S_0$ ISC; dissociation in T_1, that becomes very fast at excitation wavelengths < 306 nm; dissociation in S_1 at even shorter wavelengths. The ground state C-C bond cleavage is probably in competition with the hypothesized closed shell dissociation to C_2H_6 + CO [21]. For the isolated molecule the relative importance of the different mechanisms essentially depends on the excitation wavelength, but in gas phase collisional quenching can induce electronic transitions or

vibrational energy loss, with different efficiencies according to the nature and lifetimes of the involved states. A comprehensive kinetic model of acetone photochemistry should take into account all these aspects.

Acknowledgments

References

[1] Klessinger, M.; Michl, J. *Excited states and photochemistry of organic molecules* VCH publishers (1995).

[2] Owrutsky, J. C.; Baronavski, A. P. *J. Chem. Phys.* **1999**, *110*, 11206.

[3] Zhong, Q.; Poth, L.; Castleman, A. W. *J. Chem. Phys.* **1999**, *110*, 192.

[4] Diau, E. W.-G.; Kötting, C.; Zewail, A. H. *ChemPhysChem* **2001**, *2*, 273.

[5] Rusteika, N.; Møller, K. B.; Sølling, T.I. *Chem. Phys. Lett.* **2008**, *461*, 193.

[6] Brogaard, R. Y.; Sølling, T.I.; Møller, K. B. *J. Phys. Chem. A* **2011**, *115*, 556.

[7] Shibata, T.; Suzuki, T, *Chem. Phys. Lett.* **1996**, *262*, 115.

[8] Anner, O.; Zuckermann, H.; Haas, Y. *J. Phys. Chem.* **1985**, *89*, 1336.

[9] Zuckermann, H.; Schmitz, B.; Haas, Y. *J. Phys. Chem.* **1989**, *93*, 4083.

[10] Haas, Y. *Photochem. Photobiol. Sci.* **2004**, *3*, 6.

[11] Somnitz, H.; Fida, M.; Ufer, T.; Zellner, R. *Phys. Chem. Chem. Phys.* **2005**, *7*, 3342.

[12] Somnitz, H.; Ufer, T.; Zellner, R. *Phys. Chem. Chem. Phys.* **2009**, *11*, 8522.

[13] Martínez-Núñez, E.; Fernández-Ramos, A; Cordeiro, M. N. D. S.; Vázquez, S. A.; Aoiz, F. J.; Bañares, L. *J. Chem. Phys.* **2003**, *119*, 10618.

[14] Trentelman, K. A.; Kable, S. H.; Moss, D. B.; Houston, P. L. *J. Chem. Phys.* **1989**, *91*, 7498.

[15] Hall, G. E.; Metzler, H. W.; Muckermann, J. T.; Preses, J. M.; Weston, R. E. *J. Chem. Phys.* **1995**, *102*, 6660.

[16] North, S. W.; Blank, D. A.; Gezelter, J. D.; Longfellow, C. A.; Lee, Y. T. *J. Chem. Phys.* **1995**, *102*, 4447.

[17] Rajakumar, B.; Gierczak, T.; Flad, J. F.; Ravishankara, A. R.; Burkholder, J. B. *J. Photochem. Photobiol. A: Chemistry* **2008**, *199*, 336.

[18] Gandini, A.; Hackett, P. A. *J. Am. Chem. Soc.* **1977**, *99*, 6195.

[19] Blitz, M. A.; Heard, D. E.; Pilling, M. J. *J. Phys. Chem. A* **2006**, *110*, 6742.

[20] Szilágyi, I.; Kovács, G.; Farkas, M.; Zügner, G.; Gola, A.; Dóbé, S.; Demeter, A. *React. Kinet. Catal. Lett.* **2009**, *96*, 437.

[21] Goncharov, V.; Herath, N.; Suits, A. G. *J. Phys. Chem. A* **2008**, *112*, 9423.

[22] Koch, J. D.; Hanson, R. K.; Koban, W.; Schulz, C. *Appl. Opt.* **2004**, *43*, 5901.

[23] Antol, I.; Eckert-Maksić, M.; Ončák, M.; Slavíček, P.; Lischka, H. *Coll. Czech. Chem. Commun.* **2008**, *73*, 1475.

[24] Maeda, S.; Ohno, K.; Morokuma, K. *J. Phys. Chem. Lett.* **2010**, *1*, 1841.

[25] Liu, D.; Fang, W.-H.; Fu, X.-Y. *Chem. Phys. Lett.* **2000**, *325*, 86.

[26] Kim, S. K.; Pedersen, S.; Zewail, A. H. *J. Chem. Phys.* **1995**, *103*, 477.

[27] Nobre, M.; Fernandes, A.; Ferreira da Silva, F.; Antunes, R.; Almeida, D.; Kokhan, V.; Hoffmann, S. V.; Mason, N. J.; Eden, S.; Limão-Vieira, P. *Phys. Chem. Chem. Phys.* **2008**, *10*, 550.

[28] Baba, M.; Hanazaki, I.; Nagashima, U. *J. Chem. Phys.* **1985**, *82*, 3938.

[29] NIST Computational Chemistry Comparison and Benchmark Database, NIST Standard Reference Database Number 101 Release 15b, August 2011, Editor: R. D. Johnson III (http://cccbdb.nist.gov/). The D_e value of 3.83 eV has been obtained from the experimental reaction enthalpy at 0 K ($D_0 = 3.60 \pm 0.02$ eV) using the experimental ZPE for acetone (17775.1 cm^{-1}) and CH$_3$ (6362.3 cm^{-1}), and a calculated cc-pVTZ/CCSD(T) value for the ZPE of CH$_3$CO (9498 cm^{-1}).

[30] El-Sayed, M. A. *J. Chem. Phys.* **1963**, *38*, 2834.

[31] Test geometry optimization performed at the SS-CASSCF level for the four states S_0, S_1, T_1 and T_2 with the aug-cc-pVTZ (for C and O, without the diffuse set of f functions) and cc-pVDZ (for H) basis set gave geometrical parameters almost coincident with those obtained with the smaller basis set here considered; differences in transition energies, evaluated at S_0, S_1 and T_1 equilibrium geometries at SA-CAS and MRCI level, were always ≤ 0.02 eV.

[32] Lischka, H.; Müller, T.; Szalay, P. G.; Shavitt, I.; Pitzer, R. M.; Shepard, R. *WIREs Comput. Mol. Sci.* **2011**, *1*, 191.

[33] Werner, H.-J.; Knowles, P. J.; Knizia, G.; Manby, F. R.; Schütz, M. *WIREs Comput. Mol. Sci.* **2012**, *2*, 242.

[34] Angeli, C.; Borini, S.; Ferrighi, L.; Cimiraglia, R. *J. Chem. Phys.* **2005**, *122*, 114304.

[35] Yujing, M.; Mellouki, A. *J. Photochem. Photobiol. A: Chemistry* **2000**, *134*, 31.

[36] Gierczak, T.; Burkholder, J. B.; Bauerle, S.; Ravishankara, A. R. *Chem. Phys.* **1998**, *231*, 229.

[37] Angeli, C.; Borini, S.; Ferrighi, L.; Cimiraglia, R. *J. Mol. Struct. (THEOCHEM)* **2005**, *718*, 55.

[38] Granucci, G.; Toniolo, A. *Chem. Phys. Lett.* **2000**, *325*, 79.

[39] Ciminelli, C.; Granucci, G.; Persico, M. *J. Chem. Phys.* **2005**, *123*, 174317.

[40] Cusati, T.; Granucci, G.; Martínez-Nũnez, E.; Martini, F.; Persico, M.; Vázquez, S. *J. Phys. Chem. A* **2012**, *116*, 98.

[41] Dewar, M. J. S.; Zoebisch, E. G.; Healy, E. F.; Stewart, J. J. P. *J. Am. Chem. Soc.* **1985**, *107*, 3902.

[42] Granucci, G.; Persico, M. *J. Comput. Chem.* **2011**, *32*, 2690.

[43] Schmidt, M. W.; Baldridge, K. K.; Boatz, J. A.; Elbert, S. T.; Gordon, M. S.; Jensen, J. H.; Koseki, S.; Matsunaga, N.; Nguyen, K. A.; Su, S.; Windus, T. L.; Dupuis, M.; Montgomery, J. A. *J. Comput. Chem.* **1993**, *14*, 1347.

[44] Granucci, G.; Toniolo, A.; Persico, M. *J. Chem. Phys.* **2001**, *114*, 10608.

[45] Granucci, G.; Persico, M.; Spighi, G. *J. Chem. Phys.* **2012**, *137*, 22A501.

[46] Plasser, F.; Granucci, G.; Pittner, J.; Barbatti, M.; Persico, M.; Lischka, H. *J. Chem. Phys.* **2012**, *137*, 22A514.

[47] Granucci, G.; Persico, M. *J. Chem. Phys.* **2007**, *126*, 134114.

[48] Smeyers, Y. G.; Senent, M. L.; Botella, V.; Moule, D. C. *J. Chem. Phys.* **1993**, *98*, 2754.

[49] Klán, P.; Wirz, J. *"Photochemistry of Organic Compounds: from concepts to practice"*, J. Wiley (2009)

[50] Cusati, T.; Granucci, G.; Persico, M. *J. Am. Chem. Soc.* **2011**, *133*, 5109-5123.
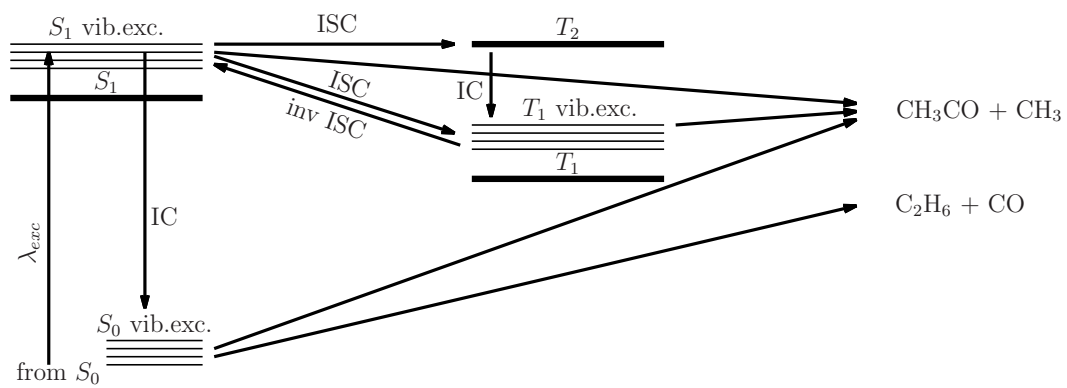
Supporting informations

Dynamics of acetone photodissociation: a surface hopping study.

Lucilla Favero, Giovanni Granucci, Maurizio Persico

We show in Tables S1–S6 the state averaged CASSCF (6 electrons/5 MOs) optimized geometries for acetone. Four states (S_0, S_1, T_0, T_1) are averaged with equal weights. Basis set: cc-pVTZ for C and O, cc-pVDZ for H. The cartesian coordinates are given in Å.

Table S1: Minimum of the S_0 state.

C	0.000000	0.000000	0.000000
C	0.000000	0.000000	1.509732
O	1.047142	0.000000	2.145328
C	−1.339319	0.000000	2.206521
H	1.016055	0.000000	−0.373413
H	−1.201640	0.000000	3.280229
H	−0.524143	−0.875814	−0.374261
H	−1.913244	−0.875814	1.914275
H	−0.524143	0.875814	−0.374261
H	−1.913244	0.875814	1.914275

Table S2: Minimum of the S_1 state.

C	0.000000	0.000000	0.000000
C	0.000000	0.000000	1.496859
O	1.293753	0.000000	2.023355
C	−0.925745	−0.882245	2.274822
H	0.650393	0.779401	−0.385914
H	−0.864661	−0.664463	3.337011
H	0.346819	−0.956526	−0.394606
H	−0.680832	−1.935890	2.130630
H	−1.004092	0.178987	−0.370797
H	−1.949378	−0.721881	1.952042

Table S3: Minimum of the T_1 state.

C	0.000000	0.000000	0.000000
C	0.000000	0.000000	1.500306
O	1.274332	0.000000	2.023051
C	-0.927925	-0.899776	2.262065
H	0.674359	0.757513	-0.387729
H	-0.850825	-0.721403	3.330316
H	0.309102	-0.967399	-0.399209
H	-0.706158	-1.951860	2.075758
H	-0.998909	0.215869	-0.365254
H	-1.952412	-0.708708	1.959165

Table S4: Minimum of the T_2 state.

C	0.000000	0.000000	0.000000
C	0.000000	0.000000	1.489920
O	1.369919	0.000000	2.047719
C	-0.922538	-0.875762	2.265695
H	0.572278	0.839873	-0.381177
H	-0.931571	-0.587727	3.312183
H	0.460873	-0.914474	-0.381734
H	-0.595358	-1.917152	2.212303
H	-1.012440	0.055062	-0.388361
H	-1.933369	-0.819174	1.873383

Table S5: S_0/S_1 MXS.

C	0.326304	0.289794	0.155477
C	-0.770697	-0.065336	1.065682
C	-1.582579	-0.022191	-2.208091
O	1.165995	0.731873	-0.551023
H	-0.445844	-0.044718	2.104299
H	-0.871717	-0.711913	-2.624400
H	-1.630185	0.588337	0.950530
H	-1.413521	1.030558	-2.337395
H	-1.079709	-1.076297	0.825137
H	-2.576337	-0.368677	-1.986532

Table S6: S_1/T_1 MXS.

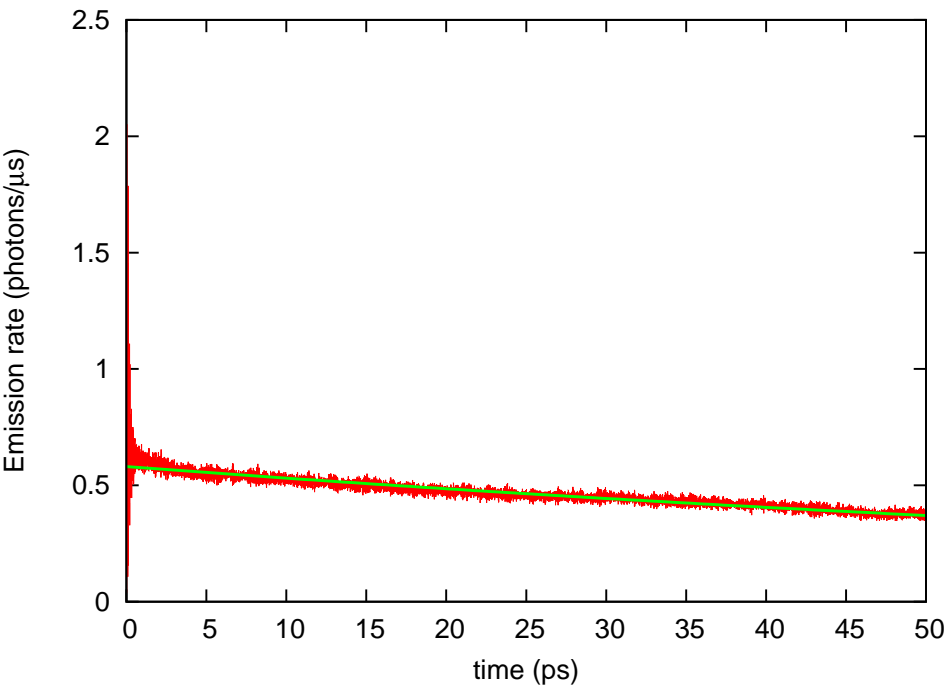|			
C	0.000000	0.000000	0.000000
C	0.000000	0.000000	1.480999
O	1.536945	0.000000	2.198341
C	-1.135175	-0.000023	2.432175
H	0.524650	0.875314	-0.378449
H	-1.088302	0.875281	3.077388
H	0.524671	-0.875302	-0.378449
H	-1.088276	-0.875335	3.077377
H	-1.005209	-0.000021	-0.405151
H	-2.091319	-0.000043	1.921899

Figure S1: Decay of the fluorescence emission rate $I_F(t)$, evaluated according to Ref. [2]. The green line is a fit with a single exponential: $I_F(t) = K_F e^{-t/\tau_{S_1}}$, with $K_F = 0.58 \ \mu s^{-1}$ and $\tau_{S_1} = 111$ ps.

Table S7: Semiempirical parameters used in this work (AM1 Hamiltonian). The names of the parameters are those used in the MOPAC 2002 documentation [1]. For the definition of β^{SCF} and β^{CI} see the text.

	units	C	O	H
U_{ss}	eV	-51.8909383808	-97.5139998672	-10.4039536311
U_{pp}	eV	-36.5021722573	-75.9645125304	
β_s^{SCF}	eV			-20.0
β_s^{CI}	eV	-13.5453111948	-28.0752048501	-9.8210776144
β_p	eV	-9.9978260863	-30.6875748839	
ζ_s	bohr^{-1}	1.6943036758	2.6628908640	1.3643861791
ζ_p	bohr^{-1}	1.6866127180	2.6641911805	
g_{ss}	eV	16.3147894450	15.6700451123	15.6659286338
g_{sp}	eV	12.2040592656	14.1791912178	
g_{pp}	eV	9.9440840041	14.5073141904	
g_{p2}	eV	8.9564330097	12.6854923108	
h_{sp}	eV	4.7177809393	3.1245676837	
α	Å^{-1}	2.4952475932	5.4104606534	2.2109546744
K_1		0.0116041336	0.2843623279	0.1179309540
K_2		0.0469381536	0.0963386154	0.0048378260
K_3		-0.0147366125		-0.0205229755
K_4		-0.0015357049		
L_1	Å^{-1}	4.1679997332	4.4460925961	5.0839087501
L_2	Å^{-1}	4.7910101173	6.9519187545	4.7537837140
L_3	Å^{-1}	5.0247436997		1.8492052033
L_4	Å^{-1}	4.8846966670		
M_1	Å	1.6837983391	0.8583319670	1.1606126823
M_2	Å	1.7810685354	1.4286432756	2.3600161003
M_3	Å	2.0756825494		2.4017376334
M_4	Å	2.7856321837		

References

[1] J. J. P Stewart, *MOPAC 2002*, Fujitsu Limited, Tokio, Japan.

[2] T. Cusati, G. Granucci and M. Persico, *J. Am. Chem. Soc.*, 2011, **133**, 5109-5123.